NUMERICAL SIMULATION AND EXPERIMENTAL INVESTIGATION OF THERMAL EFFECTS OF RF-FIELDS ON PATIENTS DURING MRI

Frank Gustrau[1] and Helmut Ermert

Ruhr-University, Institute for High-Frequency Engineering,
D-44780 Bochum, Germany

ABSTRACT. The application of radio-frequency electromagnetic fields during Magnetic Resonance Imaging causes electric currents and dielectric losses in the biological tissue of the patient during Magnetic Resonance procedures. The power deposition inside the human body leads to tissue temperature elevation. This phenomenon of whole body heating is unavoidable and of growing concern, since advanced imaging sequences as well as the trend towards high-field Magnetic Resonance scanners, lead to increased power deposition inside the human body. Therefore it becomes more and more important to incorporate the thermal aspect in the process of RF coil design. This paper presents a numerical model based on the finite element method to predict the thermo-physiological responses in human subjects during Magnetic Resonance Imaging. The simulation model includes the specific absorption rate distribution inside an anatomically shaped model of the human body, the bio-heat-transfer-equation, and a mathematical model of human thermoregulation. The model is applied to a real imaging situation and validated experimentally by temperature measurements. The comparison between experimental and numerical results shows good agreement.

1 INTRODUCTION

New pulse sequences and imaging techniques, such as magnetization transfer contrast (MTC) and turbo spin echo (TSE) and the development of high-field scanners lead to increased radio-frequency (RF) power deposition in the patient's body [1][2]. The US Food and Drug Administration (FDA) provides two options of recommended safety levels of exposure during Magnetic Resonance Imaging (MRI), which must be adhered to: either specific absorption rate (SAR) levels or temperature criteria. The temperature seems to be the more appropriate and meaningful parameter [3], whereas - from the practical point of view - it is easier to estimate the specific absorption rate. Since the SAR limit is derived from the temperature criteria under worst case conditions, in a real imaging situation the SAR criterion is more conservative than the temperature criteria.

It has been shown that temperature mapping methods are able to monitor internal body heating during magnetic resonance imaging [4]. Regardless of this capability of online-monitoring in the clinical stage of an MR-system, it is necessary to optimize the MR transmit coil in the process of technical development. The aim of the optimization is to find an acceptable compromise between requirements for high quality imaging (e.g. field homogeneity, quality factor) and tissue heating for a given application.

In this paper a numerical model of the thermal processes within the patient's body is developed. Up to now only simple models have been presented in the literature to predict whole-body thermal responses to electromagnetic field exposition in human subjects during MRI [5][6][7][8]. The calculations shown in this paper use a more detailed model based on finite element computations in an anatomically based human body model of the patient. Furthermore experimental investigations are carried out to study the dynamic response in human subjects and to validate the algorithm.

2 METHODS

The numerical model is divided into two parts: In the first step an electromagnetic model is used for the calculation of the SAR distribution for an imaging situation (frequency, whole body averaged SAR, coil design). Afterwards the time-varying temperature field inside the human body is determined based on a thermal model using the SAR distribution as a heat source and taking into account human thermoregulation.

2.1 Electromagnetic Analysis

During an MRI imaging procedure three kinds of electromagnetic fields are applied: a homogeneous static magnetic field, switched gradient fields and pulsed radio-frequency fields. The biological effects of the static

[1] Now at IMST GmbH, Kamp-Lintfort, Germany

magnetic field are non-thermal [9]. For many new and RF-intensive sequences this is also true for the switched gradient fields during conventional imaging sequences. On the other hand there are imaging sequences which apply rapidly switched gradient fields (e.g. Echo-Planar-Imaging). At the current stage of the investigation the attention is limited to the RF fields and considers only RF-coil design. Therefore, possible thermal effects caused by more rapidly changing gradient fields are beyond the scope of this paper. The safety of gradient fields cannot be assessed only from thermal considerations since possible stimulation of muscles and nerves has to be taken into account in the low frequency range [1]. The SAR distribution caused by this more rapidly switched gradient fields can be included easily in the thermal analysis by adding the corresponding specific absorption rate.

For the electromagnetic analysis a commercial finite element software package (EMAS™, Version 3.2b, Ansoft Corporation, USA) is used. The software is running on a IBM RS6000/550 workstation with 256 MB RAM. The finite element method allows a flexible mesh generation, which is necessary to model the complex biological structures of the body. A homogeneous model (muscle tissue, 7652 hexahedra, 6127 points) and a inhomogeneous model (muscle, heart, kidney lung, stomach, and liver tissue, 51716 tetrahedrons, 8476 points) are generated to investigate the influence of the body shape and tissue distribution on the distribution of the SAR. The dielectric properties of the different tissues are given in Table 1.

Tissue	ε_r	σ [S/m]
Muscle	72	0.8
Heart	100	0.6
Kidney	115	0.9
Lung	27	0.24
Stomach	40	0.35
Liver	88	0.58

Table 1: Dielectric properties (relative permittivity ε_r and conductivity σ) of different tissues at 63.6 MHz.

Since the MR pulse sequences have a narrow bandwidth, and the pulse repetition times are short in comparison to the heat transfer process, a monofrequent (AC) analysis is carried out. This method does not distinguish between different pulse sequences as long as their time-averaged power is the same. The specific absorption rate *SAR* is calculated from the distribution of the phasor of the peak value of the electric field E by

$$SAR = \frac{\sigma |E|^2}{2\rho} \tag{1}$$

where the tissue has mass density ρ and electric conductivity σ.

2.2 Thermal Analysis

The heat-transfer processes within the patient's body are modeled by the classical bio-heat-transfer equation [10]

$$c_p \rho \frac{\partial T}{\partial t} = \nabla(\lambda \nabla T) + \beta \rho_a c_a \xi (T_a - T) + \rho (MR + SAR) \tag{2}$$

with the temperature of tissue T, the time t, the specific heat capacity c_p, the thermal conductivity λ, the specific heat of arterial blood c_a, the mass density of arterial blood ρ_a , and the perfusionrate ξ. This approach represents a continuum model, which takes into account the blood perfusion as a heat source or a heat sink, depending on the difference of the local temperature of the tissue T and the global arterial temperature T_a. The architecture of the vascular system is not modeled explicitly. The heat loss due to countercurrent arterial and venous vessels is taken into consideration by introducing a countercurrent factor β [10]. Eq. (2) contains two types of heat sources, i.e. the metabolic heat generation (*MR*) and the specific absorption rate (*SAR*).

The arterial temperature is dependent on time and determined by the following heat-balance-equation [10]

$$m_a c_a \frac{dT_a}{dt} = \iiint_{body} \beta \rho_a c_a \xi (T_a - T) dv - R_R \tag{3}$$

with the mass of the arterial blood pool m_a and the term R_R for respiratory heat loss.

With regard to the mathematical model of human thermoregulation [10], the finite element model of the patient's body is subdivided into six regions (head, trunk, arms, legs, hands, feet), each consisting of a core and a shell region.

At the surface of the model we applied Cauchy boundary conditions to describe the thermal heat transition between the body and the surrounding air. The heat lost to the environment is proportional to the heat transfer coefficient α and the temperature difference between the ambient temperature T_{amb} and the tissue surface temperature T

$$\dot{q} = \alpha (T - T_{amb}) \quad . \tag{4}$$

The heat transfer coefficient α includes four heat loss mechanisms: α_r for radiation, α_{cd} for conduction, α_{cv} for convection, and α_e for evaporation

$$\alpha = \alpha_r + \alpha_{cd} + \alpha_{cv} + \alpha_e \quad . \tag{5}$$

The heat transfer coefficients for convection and evaporation depend on the velocity of air v [10]. The evaporative heat lost to the environment is not dependent on the temperature difference $(T\text{-}T_{amb})$, but on the difference between vapor pressure of air and surface. In order to facilitate the implementation of the boundary condition into the finite element algorithm, the evaporative heat loss can be calculated from the known heat loss P_e [10] and transformed into an effective evaporative heat transfer coefficient α_e given in Eq.(6)

$$\alpha_e = \frac{P_e}{A\left(T - T_{amb}\right)} \quad . \tag{6}$$

In order to solve the partial differential equation with initial and boundary conditions, a finite element algorithm is implemented. The same finite element mesh that is used for the analysis of the electromagnetic fields inside the human body is also used in the thermal analysis.

The finite element formulation is based on the Galerkin method. The partial differential equation is multiplied by a test function w, integrated over the volume Ω, and Green's formula is applied. After dividing the volume Ω into N tetragonal subvolumes Ω_i and including the Cauchy boundary conditions, the weak form of the differential equation is

$$\sum_{i=1}^{N}\Bigg[\lambda_i \iiint_{\Omega_i}\left(\frac{\partial T}{\partial x}\frac{\partial w}{\partial x}+\frac{\partial T}{\partial y}\frac{\partial w}{\partial y}+\frac{\partial T}{\partial z}\frac{\partial w}{\partial z}\right)dx\,dy\,dz$$
$$-\left(\rho(MR+SAR)+\xi\rho_a c_a T_a\right)$$
$$\times\iiint_{\Omega_i} w\,dx\,dy\,dz+\rho_i c_{p,i}\iiint_{\Omega_i}\frac{\partial T}{\partial t}w\,dx\,dy\,dz$$
$$+\xi\rho_a c_a\iiint_{\Omega_i} T\,w\,dx\,dy\,dz+\iint_{\partial\Omega}\alpha\left(T-T_u\right)w\,dA\Bigg]=0 \tag{7}$$

A linear approximation of T and w leads to Eq. (8) and (9).

$$T(x,y,z,t) = c_1(t) + c_2(t)x + c_3(t)y + c_4(t)z \tag{8}$$

$$w(x,y,z) = d_1 + d_2 x + d_3 y + d_4 z \tag{9}$$

After integration of each element and compilation of the resultant matrices the following equation can be obtained

$$\sum_{i=1}^{N}\left[T_{e,i}^T\mathbf{S}_{e,i}w_{e,i} - w_{e,i}^T b_{e,i} + \dot{T}_{e,i}^T\mathbf{M}_{e,i}w_{e,i}\right] \tag{10}$$
$$= T^T\mathbf{S}w - w^T b + \dot{T}^T\mathbf{M}w = 0$$

where $\mathbf{S}_{e,i}$ is the stiffness matrix for each element, $\mathbf{M}_{e,i}$ the mass matrix, and $b_{e,i}$ the load vector. The superscripted letter T denotes a transpose vector and the dot (•) denotes time derivative. This set of ordinary differential equations can be rewritten in the following form

$$\mathbf{S}T + \mathbf{M}\dot{T} = b \tag{11}$$

where the stiffness matrix $\mathbf{S}$ and the mass matrix $\mathbf{M}$ are both $N \times N$ matrices. This set of ordinary differential equations is solved by an iterative finite difference method, replacing the time derivative quotient by a time difference quotient. The temperature can be calculated recursively by the following formula

$$\left(\mathbf{M}+\Delta t_n \Xi\mathbf{S}\right)T(t_{n+1})$$
$$=\left(\mathbf{M}+\Delta t_n(1-\Xi)\mathbf{S}\right)T(t_n) \tag{12}$$
$$+\Delta t_n\left(\Xi\, b(t_{n+1})+(1-\Xi)b(t_n)\right)$$

where Ξ can be chosen between 0 and 1. The cases Ξ=1 and Ξ=0 are well-defined as the forward and backward Euler methods, respectively. In the simulations Ξ=½ is chosen. This case is known as the Crank-Nicolson method [11].

The appropriate implementation of the algorithm is proven by comparing the numerical results with analytical results from [12] for the cooling process of a sphere from the initial temperature of 20°C towards the ambient temperature of 0°C. In Fig. 1 the comparison between the simulation and theory for the transient center and surface temperature of the sphere is shown. The model parameters are: λ = 20 W/(m·K), radius of the sphere r = 1m, and α= 20 W/(m²·K). The simulations parameters are: 845 points, 3993 tetrahedrons and time step Δt = 10s.

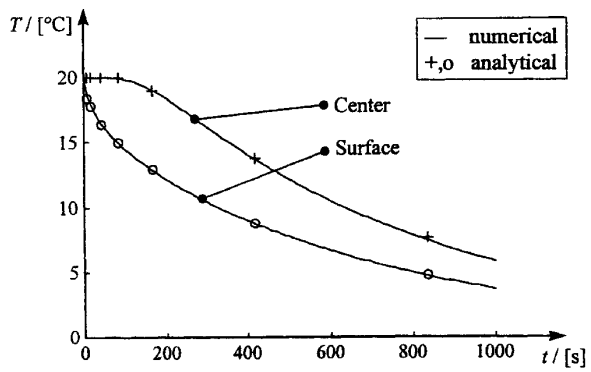

Fig. 1. Cooling of a sphere for validation of the thermal FEM algorithm.

2.3 Thermoregulation

In order to account for the physiological response of a patient undergoing thermal stress, a mathematical model

of human thermoregulation [10] is added. During heat stress two effector mechanisms of thermoregulation have to be considered: a change in skin blood flow ξ and an increased evaporative heat loss by sweating. The sweating is modeled by an increase in evaporative heat loss P_e (see Eq. (6)).

The thermoregulatory effector mechanisms are controlled by a weighted value $a(t)$ of the overall body temperatures

$$a(t) = \iiint_{body} g(\vec{r})T(\vec{r})\,dx\,dy\,dz - a_0 \qquad (13)$$

with the weighting function g and the equilibrium value a_0. Local effector mechanisms that depend only on local tissue temperature are not taken into consideration. The changes of perfusion rate $\Delta\xi$ and evaporative heat loss $\Delta\alpha_e$ are calculated by the multiplication of the afferent signal $a(t)$ with a distribution factor c_ξ for blood flow and a factor c_e for evaporative heat loss.

$$\begin{aligned} \Delta\xi &= c_\xi(\vec{r})a \\ \Delta\alpha_e &= c_e(\vec{r})a \end{aligned} \qquad (14)$$

The complete set of parameters has been presented in [10].

3 NUMERICAL RESULTS

The numerical approach is applied to the RF-system of a commercial MR-scanner, with a quadrature transmit body coil (diameter $d_c = 55$ cm; length $l_c = 90$ cm) within a cylindrical RF-shield (diameter $d_s = 67$ cm; length $l_s = 220$ cm) shown in Fig. 2. A model of the patient's body is placed inside the magnet bore. Due to the cut-off effect of a cylindrical hollow wave guide RF shield the electromagnetic field decays strongly in the axial direction (z-direction). Hence, both ends of the tube can be modeled by magnetic walls as appropriate boundary conditions, and the surroundings of the MR-scanner need not be considered in the modeling process.

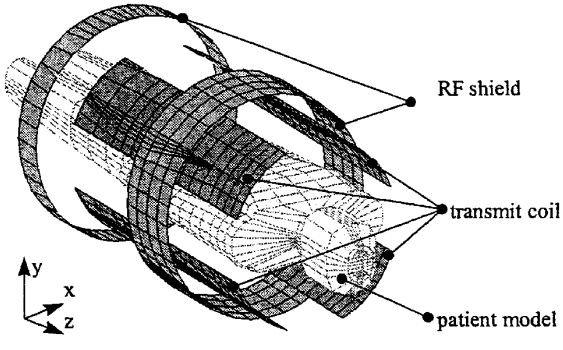

Fig. 2. Geometry of the quadrature RF-system

3.1 SAR Distribution

Figs. 3 - 4 present the simulation results for $f = 63.6$ MHz and a time-averaged whole body averaged SAR of 3 W/kg in a homogeneous patient model with the following material properties: dielectric properties of muscle tissue (see Table 1) relative permeability $\mu_r = 1$, and mass density $\rho = 1000$ kg/m³. In Fig. 3 the distribution of the specific absorption rate on the surface of the body is shown. The main power deposition is restricted to the area of the body that is placed within the length of the transmit coil. Fig. 4 shows the specific absorption rate in a transversal plane through the body at the navel. Within the trunk the power deposition grows with increased distance from the longitudinal body axis (z-axis). The interaction between the induced eddy currents and the incident electromagnetic field results in an asymmetric placement of the maximum local power deposition at the lateral side of the trunk. The maximum SAR occurs at the surface of the body.

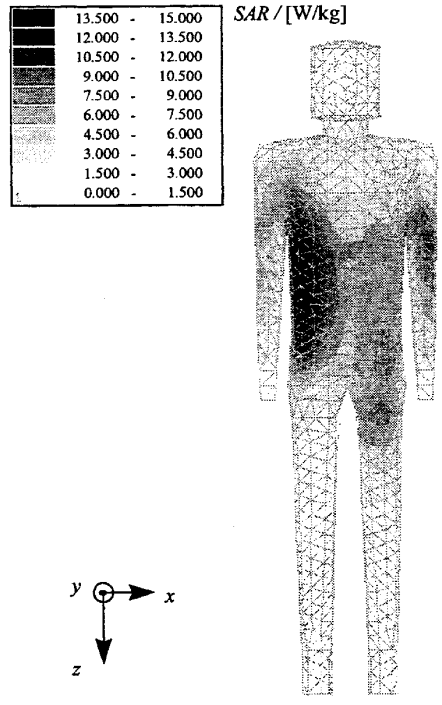

Fig. 3. Calculated specific absorption rate on the surface of the body.

Comparisons are made between homogeneous and inhomogeneous models. The number of cells for each model ranges from 10,000 to 50,000 finite elements. The homogeneous model consists of muscle tissue only. The inhomogeneous model is composed of different tissues. The tissues and dielectric properties of the

inhomogeneous model are listed in Table 1. A non-uniform distribution of different tissues can cause focal heating, as demonstrated by [13] in a phantom study. The investigation in our study showed that the inhomogeneous tissue distribution makes little influence on the distribution of the specific absorption rate: no hot-spots within the body or within special organs are detected. This result agrees well with findings in [7][8]: even simulations with detailed torso models containing several tissues showed no hot-spots. The RF radiation is mainly absorbed by peripheral tissues [2] [7]. It should be pointed out that the individual anatomy varies from patient to patient and hence it is not possible to model its whole variety. However, in order to make predictions of the thermal behavior for a standard patient, it is reasonable to simplify the problem for a first approach and to narrow down the broad variety of anatomies to a single homogeneous model.

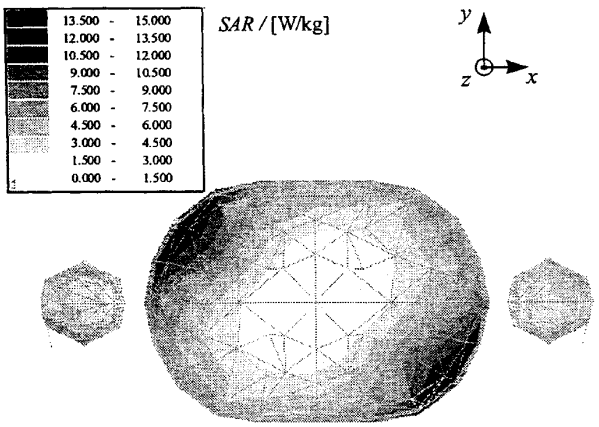

Fig. 4. Calculated specific absorption rate in a transversal plane near the navel.

3.2 Steady State Temperature Field

Without RF irradiation and under constant environmental conditions, the temperature field within the patient's body is time-invariant. The calculated steady state temperature field in the *xz*-plane of the body model is shown in Fig. 5 for an ambient temperature of $T_{amb} = 20°C$. In the core region of the trunk and head we see a homogeneous temperature distribution with temperatures between 36°C and 37°C. In the limbs the temperature decays in the axial and radial direction. This results agree well with the physiological literature [14] and shows that with the chosen parameter values an accurate initial temperature for the following transient thermal analysis is obtained.

3.3 Transient Temperature Fields

During RF exposure the temperature distribution within the human body increases. Fig. 6 shows the time-variant temperatures at three different locations: navel temperature, temperature at the side of the trunk (in the region of maximum local SAR), and core temperature. The exposure conditions are as follows: whole body averaged $SAR = 3$ W/kg, duration of exposure $\Delta t = 20$ min, ambient temperature $T_{amb} = 20°C$, relative humidity of air 45%, air velocity $v = 0.05$ m/s. The solid lines indicate the simulation results including thermoregulatory effects. The dashed lines show the simulation results without thermoregulation. The temperature plots for the side of the trunk without thermoregulation is left out for clarity.

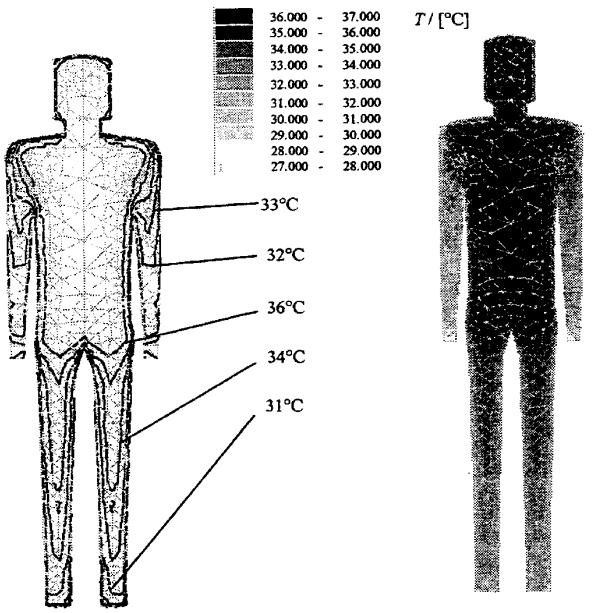

Fig. 5. Steady-State Temperature Field (xz-plane) within the patients body without RF irradiation.

During RF exposure a temperature rise at all locations is observed. When thermoregulation is considered, the temperatures return to the steady-state values after the exposure, whereas, when thermoregulation is neglected, the temperature decreases very slowly and seems to approach a different value. The core temperature continues to increase until it reaches a maximum temperature change of about 1°C. This value can also be explained as follows: due to the RF-induced heat load of 3 W/kg and a duration of exposure of $\Delta t = 20$ min, we expect an increase of the overall temperature of about 1°C for a passive system and a homogeneous power deposition according to the following formula taken from [15] with $c_p = 3300$ J/(kg·K).

$$\Delta T = \frac{SAR\,\Delta t}{c_p} \approx 1°C \tag{15}$$

After some time the perfusion of the tissue leads to a homogeneous distribution of the RF-induced heat. The heat loss to the environment is adjusted to dissipate the metabolic heat of about 1.15 W/kg. Consequently, the additional heat is stored in the body and leads to a temperature increase of about 1°C as mentioned above. Without thermoregulation the additional heat will be dissipated to the environment more slowly by an increase of body surface temperature.

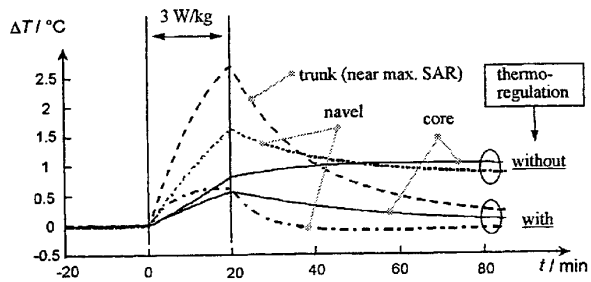

Fig. 6. Simulated transient temperature plots at three different locations: navel, side of the trunk (near maximum local SAR) and core. Solid lines indicate simulation results including thermoregulation, dashed lines show simulation results without thermoregulation.

4 VALIDATION

For experimental validation of the numerical simulation measurements have been performed. Measurements within the vicinity of a real clinical scanner are difficult to make because of the interference of the strong magnetic field with the laboratory equipment (e.g. network analyzer). As discussed during the electromagnetic analysis, the static magnetic field does not contribute to the temperature effects of the RF fields. Furthermore this investigation is limited to the RF fields. Hence, the experiments are performed using an RF system without a magnet and gradient system.

4.1 Experimental Setup

Fig. 7 shows the experimental setup. The main component of the setup is a commercial RF-system of a 1.5 T scanner including quadrature RF transmit body coil (R), RF shield, patient table (P), tuning and matching circuits (MA 1, MA 2), and hybrid power divider. The setup also includes a power meter, a broadband amplifier and a signal generator. The system is driven by a continuous wave (CW) signal with $f = 63.6$ MHz. Before starting the exposure the loaded quality factor Q_L and the unloaded quality factor Q_0 of the RF transmit system are measured using a network analyzer in order to determine the fraction of power P_{pat} that is absorbed by the patient.

$$P_{pat} = P_{in}\left(1 - \frac{Q_L}{Q_0}\right) \tag{16}$$

P_{in} is the total power fed into the RF system. During the experiment the temperature at two locations of the patient's body is monitored using a two-channel fiber-optic temperature measurement device (Luxtron 712) and a personal computer. The fiber-optic thermometry system allows an unperturbed measurement of temperatures in a RF electromagnetic environment [1]. With this device we measured skin temperatures and sublingual temperature. Skin temperature was obtained by attaching the temperature probe to the surface of the skin with tape [1].

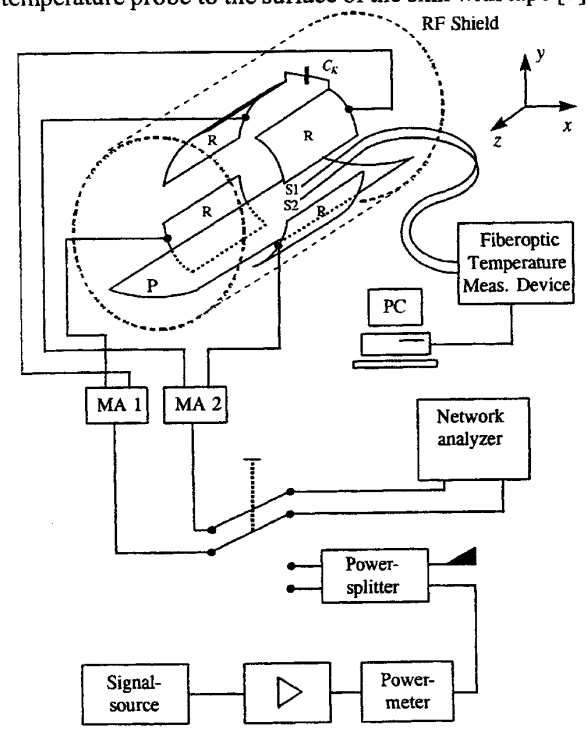

Fig. 7. Experimental set-up including patient table (*P*), fiber-optic temperature probes (*S1*, *S2*), decoupling capacitor (C_K), quadrature transmit coil with four resonators (*R*), and tuning and matching circuits (*MA 1*, *MA 2*).

Ten young (age: 21-29 years), healthy, and not obese volunteers with normal thermoregulatory function served as subjects. These volunteers were located with their navel in the isocenter of the RF-system. This position has been used by other authors in order to assess thermal effects of RF fields during MRI [1] [15] [16].

Before starting the irradiation the subjects were exposed to constant ambient conditions in order to wait for steady-

state temperatures. The room temperature ranged from 20°C to 24°C, depending on the time of day at which the experiment was conducted, but was constant (±0.1°C) for each measurement. The relative humidity ranged from 40% to 50 %, and the air velocity was less than 0.1 m/s. After this equilibrium interval, the subjects were exposed to the electromagnetic field that induced a whole body averaged SAR of 3 W/kg for 20 minutes. The subjects were told not to move for two reasons: to simulate a real MR imaging situation and not to effect the tuning of the transmit coil and the corresponding power deposition.

4.2 Experimental Results

The temperature changes measured at several locations of the bodies of the ten volunteers are compiled in Table 2. The maximum temperature changes are: 1.6°C in the vicinity of the navel, 3.2°C at the right side of the trunk (near maximum SAR (see Fig. 3)), 1.3°C at the left side of the trunk, and 1.9°C at the upper right arm. The measured maximum sublingual temperature change was 0.15°C.

Volunteer	Position	ΔT/[°C]
1	vicinity of the navel	0.55
	air at isocenter	0.4
2	vicinity of the navel	1.1
	air at isocenter	0.5
3	vicinity of the navel	0.9
	sublingual	0.0
4	trunk lateral (left)	0.5
	trunk lateral (right)	2.1
5	vicinity of the navel	1.6
	trunk lateral (right)	1.8
6	vicinity of the navel	1.2
	trunk lateral (right)	1.7
7	trunk lateral (right)	1.2
	right upper arm	1.9
8	trunk lateral (left)	1.3
	trunk lateral (right)	3.2
9	trunk lateral (right)	1.3
	right upper arm	1.7
10	vicinity of the navel	1.4
	sublingual	0.15

Table 2: Maximum temperature changes in 10 volunteers for a whole body averaged SAR of 3 W/kg and a duration of irradiation of 20 minutes.

The subjects showed visible signs of sweating on their foreheads after 5 to 10 minutes and reported a significant feeling of warmth in the trunk. Two subjects reported an additional feeling of warmth in the region of their shoulders and upper arms. This may be explained by the proximity of this region to the conductors of the transmit coil. None of the volunteers reported feeling uncomfortable.

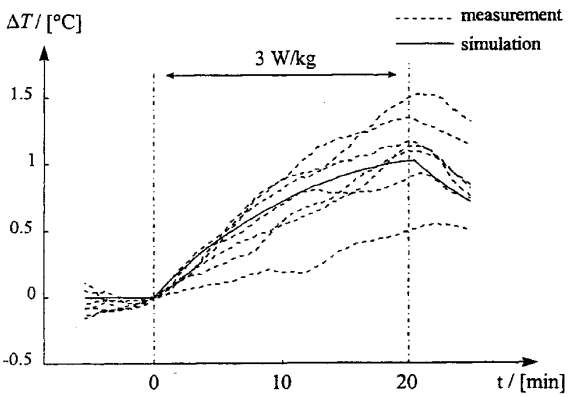

Fig. 8. Experimental results (dashed lines) and simulated curve (solid line) for the superficial temperature in the vicinity of the navel.

The experimental results for the transient temperatures in the vicinity of the navel are shown in Fig. 8. The dashed lines represent the temperature change over time for six individuals, and are compared to the simulated temperatures indicated by the solid line. The considerable span of the measured temperature curves reflects intra- and inter-individual differences and lack of exact initial steady-state temperatures. Diurnal variations in human body temperature may also effect the measured temperature change.

The experimental results agree well with published results [16]. Using a slightly different MR system with a shorter body coil (55 cm) and comparable whole-body averaged SAR (2.8 W/kg to 4 W/kg, exposure time 30 min) no significant body temperature changes (<0.2°C) but significant skin temperature changes (up to 3.9°C) were measured.

Skin temperature changes measured in our investigation are significantly greater than in [15] due to the higher air flow velocity in [15]. Our measurement reveals a rise in ambient temperature (about 0.4–0.5°C) without air flow, which indicates a heat accumulation within the bore of the magnet. Consequently, in order to keep skin temperature changes low it is recommended that an air flow through the tube be generated by a ventilating fan to increase heat loss via convection.

However, the objective of our measurement was to validate the algorithm. As seen in Fig. 8, taking into account the uncertainty of the measurements mentioned above, the absolute temperature changes and the dynamics of the heat transfer process is described adequately by the numerical model.

5 CONCLUSIONS

We introduced a numerical model that is capable of predicting transient temperature in the human body caused by RF exposure during MRI. The model was applied to a commercial MR scanner. The numerical results were validated with experimental data and compared with other studies in the literature. The model predicted transient temperatures that are within the experimental range. The experimental data and numerically predicted temperature curves were in good agreement.

ACKNOWLEDGEMENT

The authors would like to thank Dr. Wilhelm Dürr and Dr. Wolfgang Renz, Siemens AG, Medical Engineering, Erlangen, Germany for providing the RF-System of a clinical MR scanner and for many helpful discussions.

This work was supported by the German Research Association (*Deutsche Forschungsgemeinschaft*) through grant Er 94/13.

REFERENCES

[1] F.G. Shellock, D.J. Schaefer, E. Kanal, Physiologic Responses to an MR-Imaging Procedure Performed at a Specific Absorption Rate of 6.0 W/kg. *Radiology*, **192**, 865–868 (1994).

[2] F.G. Shellock, Radiofrequency Induced Heating During MR Procedures: A Review. *Journal of Magnetic Resonance Imaging*, **12**, 30–36 (2000).

[3] F.G. Shellock, E. Kanal, Magnetic Resonance, Bio-effects, Safety, and Patient Managing. Raven Press, New York, 1994.

[4] Y. Ishihara et al. Monitoring Internal Body Heating Induced by Radio-Frequency Irradiation - Comparison of Measured Temperature Changes and SAR Distribution Computed Numerically -. *Proceedings Int. Soc. Magn. Reson. Med.*, Vancouver, 1953 (1997).

[5] E.R. Adair, L.G. Berglund, Predicted Thermo-physiological Responses of Humans to MRI-Fields, in R.L. Magin, R.P. Liburdy, B. Persson (Eds.), *Biological Effects and Safety Aspects of Nuclear Magnetic Resonance Imaging and Spectroscopy*, New York Academy of Sciences, New York, 188–200 (1992).

[6] C.J. Gordon, Local and Global Thermoregulatory Responses to MRI Fields, in R.L. Magin, R.P. Liburdy, B. Persson (Eds.), *Biological Effects and Safety Aspects of Nuclear Magnetic Resonance Imaging and Spectroscopy*, New York Academy of Sciences, New York, 273–284 (1992).

[7] D. Simunic, Thermal and Stimulating Effects of Time-Varying Magnetic Fields during MRI, Ph.-D. Thesis, Technische Universität, Graz, 1995.

[8] D. Simunic, P. Wach, W. Renhart, R. Stollemberger, Spatial distribution of high-frequency electromagnetic energy in human head during MRI: numerical results and measurements, *IEEE Trans Biomed Eng.* , **43**(1), 88–94 (1996).

[9] F.G. Shellock, D.J. Schaefer, C.J. Gordon, Effect of a 1.5 T Static Magnetic Field on Body Temperature of Man. *Magnetic Resonance in Medicine*, **3**, 644–647 (1986).

[10] J. Werner, P. Webb, A Six-cylinder Model of Human Thermoregulation for General Use on Personal Computers, *The Annals of Physiological Anthropology*, **12**(3), 123–134 (1993).

[11] A. Quarteroni, A. Valli, Numerical Approximation of Partial Differential Equations, Springer, Berlin, 1994.

[12] W. Wagner, Wärmeübertragung, Vogel Buchverlag, Würzburg, 1993.

[13] P.L. Davis, C. Shang, L. Talagala, A.W. Pasculle, Magnetic Resonance Can Cause Focal Heating in a Nonuniform Phantom, *IEEE Trans. Biomed. Eng.*, **40**(12), 1324–1327 (1993).

[14] J. Aschoff, Temperaturregulation, in Gauer/Kramer/Jung (Eds.) *Physiologie des Menschen*, Band 2, Urban und Schwarzenberg, München, 43–116 (1971).

[15] J. Abart, G. Brinker, W. Irlbacher, J. Grebmeier, Temperature and Heart Rate Changes in MRI at SAR Levels of up to 3W/kg, Reprint of a Poster Presented at the 8th Annual Meeting, Society of Magnetic Resonance in Medicine, Amsterdam, 1989.

[16] F.G. Shellock, D.J. Schaefer, J.V. Crues, Alterations in Body and Skin Temperature Caused by Magnetic Resonance Imaging: is the Recommended Exposure for Radiofrequency Radiation too Conservative? *British Journal of Radiology*, **62**, 904–909,1989.